Materials and Design 85 (2015) 412–422

Contents lists available at ScienceDirect

Materials and Design

journal homepage: www.elsevier.com/locate/jmad

Effect of WC particle size and Ag volume fraction on electrical contact resistance and thermal conductivity of Ag–WC contact materials

Nachiketa Ray [a,*], Bernd Kempf [b], Timo Mützel [b], Ludo Froyen [a], Kim Vanmeensel [a], Jef Vleugels [a]

[a] Department of Materials Engineering, KU Leuven, Kasteelpark Arenberg, 44, 3001 Leuven, Belgium
[b] Umicore AG & Co. KG, Rodenbacher Chaussee 4, 63457 Hanau-Wolfgang, Germany

ARTICLE INFO

Article history:
Received 10 April 2015
Received in revised form 8 June 2015
Accepted 1 July 2015
Available online 8 July 2015

Keywords:
Metal-matrix composite
Electrical contact
Infiltration
Contact resistance
Thermal conductivity
Thermal stress cracking

ABSTRACT

In this work, theoretically dense (>99%) composites of Ag and WC have been prepared by press–sintering–infiltration for making electrical contacts used as an arc-resistant material in a model switching device. Composites with varying silver content and WC particle size were investigated to get an insight on their electrical contact resistance (R_c) and their ability to withstand enormous thermal stresses during switching. A break-only model switching sequence was used, where the evolution of R_c was measured over 50 cycles and the post-switching microstructures were investigated for thermal stress induced crack formation. A well-established 2D computational microstructure based model, object-oriented finite element analysis version 2 (OOF2), was used to determine the composite thermal conductivity (k) for various grades as a function of temperature. R_c was observed to be consistently low for the coarser WC containing composite and higher silver content composites. This response was attributed to the ductility of the surface layers formed during switching. Crack formation after switching was found to be a direct consequence of large thermal gradients during 50 cycles, which was minimal for coarser WC grained and higher silver content composites which have a higher thermal shock resistance.

1. Introduction

Silver based metal matrix refractory composites have been of considerable interest to the electrical industry for making electrical contacts, which are employed in circuit breakers [1–3] and vacuum contactors [3,4] as an arc-resistant material. The addition of refractory carbides and/or metals like WC and W to the silver matrix has resulted in enhancing the desired properties of these materials. Opposed to true alloys, there is no or limited solubility of silver in the refractory phase, thus the individual phases retain their respective thermal and electrical properties [5]. These electrical contacts are produced via powder metallurgical routes which generally involve press–sinter–infiltration, press–sinter (in solid phase)–repress and press–sinter (in liquid phase). One of the important properties that determine the switching behavior of these materials is the electrical contact resistance (R_c), which is a combination of *constriction resistance* and resistance from *contaminant films* on the interface, and bulk resistance. However, the larger contribution of resistance comes from the constriction of the electric current through the spot contacts (also called *a*-spots). There are several mathematical models to predict the actual area of contact or the area fraction of the *a*-spots on the surface.

For a single circular constriction of radius a, the constriction resistance between two pure metals of resistivity ρ_1 and ρ_2 can be written as [6]

$$R_c = \frac{(\rho_1 + \rho_2)}{4a}. \tag{1.1}$$

More terms are added to the above expression depending on the aspect ratio and complexity of the constriction shape. In practice, an electrical junction comprises a multitude of contact *a*-spots through which the electric current is constricted. The number of asperity contacts depends directly on the contact load (F) and inversely on the plastic flow stress (or hardness) (H) of the material. The area of true mechanical contact (A_c) can be written as

$$A_c = \frac{F}{H}. \tag{1.2}$$

Assuming that n number of circular *a*-spots are present on a contact surface having a mean *a*-spot radius a ($= \sum a_i/n$), where a_i is the radius of the ith spot. Then the radius of such a cluster of spots is defined as the Holm radius (α) (Fig. 1) and the constriction resistance between the two mating surfaces can be written as [7]

$$R_c = (\rho_1 + \rho_2)\left(\frac{1}{4na} + \frac{1}{4\alpha}\right). \tag{1.3}$$

* Corresponding author.
E-mail addresses: nachiketa.ray@mtm.kuleuven.be, nachiketa.ray.1014@gmail.com (N. Ray).

http://dx.doi.org/10.1016/j.matdes.2015.07.006
0264-1275/

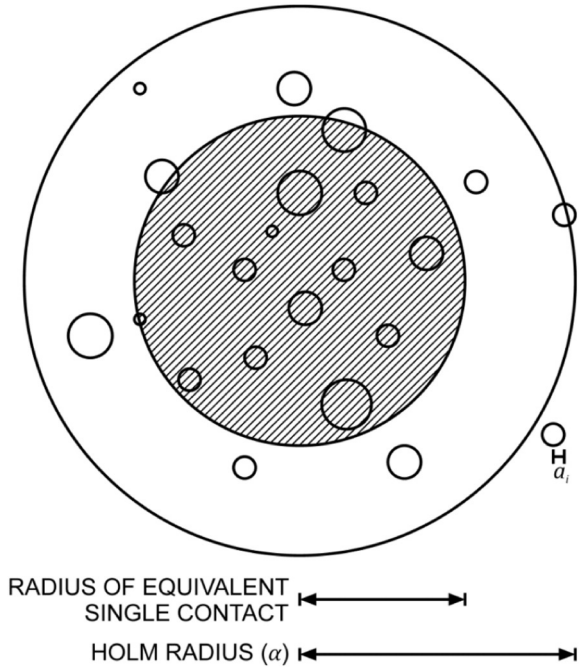

Fig. 1. Cluster of *a*-spots showing the radius of equivalent contact and Holm radius (α) (redrawn from [4]).

Experimental investigations suggest that the second term in Eq. (1.3) is more dominant when $a > 0.05$ units. Hence for most engineering purposes the knowledge of the Holm radius is sufficient to estimate the electrical contact resistance. As a result the area of true mechanical contact (A_c) would be ($=\eta\pi\alpha^2$) where η is an empirical coefficient of unity order for clean interfaces. By combining Eqs. (1.2) and (1.3), the electrical contact resistance (R_c) can be expressed as

$$R_c = \frac{(\rho_1+\rho_2)}{4}\sqrt{\frac{\eta\pi}{A_c}} = \frac{(\rho_1+\rho_2)}{4}\sqrt{\frac{\eta\pi H}{F}}. \quad (1.4)$$

It is very important to note that the electrical contact resistance (R_c) is independent of the area of nominal contact of the two surfaces and depends only on A_c which is a function of the contact force and hardness (see Eq. (1.2)). Thus two contact pairs, made of identical materials with exactly the same surface finish subjected to the same contact force will end up having identical values of contact resistance, independent of the diameter of the contact.

Now we can appreciate that apart from bulk resistivity, ductility and true area of mechanical contact significantly contributes to the contact resistance. As discussed earlier, these electrical contacts are metal matrix composites, which have inherent soft and hard phase's properties.

Predicting the conductivity of particulate composites through analytical and numerical methods has been of interest in the last few decades due to numerous possibilities of having tailor made electrical and thermal properties. Most of the theories are based on either an effective medium approach [8,9] or percolation model [10] and some of them even combine some aspects from both the theories which were applicable to systems characterized by a strong percolation effect [11]. It is quite obvious that the resistivity of the composite decreases with increasing silver content and the hardness increases with addition of tungsten carbide [12]. In this work we simulated the composite thermal conductivity in order to visualize the percolation effect. Object-oriented finite element analysis version 2 (OOF2) [13,14], an open access software developed at the National Institute of Standards and Technology (NIST), was used to generate a thermal gradient model to calculate the effective thermal conductivity (k) for different compositions and WC particle sizes as a function of temperature. OOF2 uses two-dimensional microstructures with significant contrast as input geometry for the finite element calculations, which has been successfully used before for determining thermal properties of two-phase composites [15,16] and thermal barrier coatings [17].

However, switching is a very dynamic process, which results in significant changes in the surface layers, which makes it difficult to predict the contact resistance, R_c. Although Eq. (1.4) allows predicting the initial contact resistance at the interface between two contacts, this prediction is limited to pristine contacts since the topology of the interface changes and the hardness of the surface would be non-uniform and different from the bulk hardness after the first arc strikes.

Several silver-based contact materials (Ag–WC, Oxides, Cu, Ni) are used for specific switching applications. Jaćimović [18] provided a comparison of different silver-based contact materials, tested under direct current (DC) which involves a directional material transfer between the electrodes. In this work, we only focus on contacts for AC circuit breakers, where the electrodes switch polarity after each cycle and material loss from each electrode would be similar.

Before thinking in terms of a complex composite material, the work of Slade [19] provides a platform to understand the contact resistance evolution of pure materials. He compared the temperature rise in contacts made of pure Ag, pure W and Ag/W 35/65 wt.% with a thin layer of Ag. For un-arced contacts, R_c of Ag < Ag–W < W; whereas after arcing, R_c of Ag < W < Ag–W [11]. The lower contact resistance for un-arced Ag–W contacts was due to the thin silver layer on the surface. His work motivates us to design Ag-based contacts with very stable contact resistance after several operations at overload current.

Table 1 gives an overview of the relevant switching tests done on Ag–WC contact materials by several researchers. The switching test conditions used in each case are very distinct, thus prudence is required to compare different results. The Ag content has only been varied in [1], and dopant amount has been varied in [2], whereas the effect of the WC particle size or the reinforcing phase has never been studied. Thus in this work, we study the influence of both the WC particle size and Ag content on the contact resistance of Ag–WC contact materials.

2. Experimental procedure

2.1. Starting powders and densification

The shape of electrical contacts varies according to their application from very simple shapes like discs to complicated non-geometrical shapes. In this work, 7 mm diameter discs were produced by powder compaction followed by infiltration. In this process a powder mixture of Ag and WC was pre-compacted to form a porous network which was later infiltrated with molten silver.

WC powders of three particle sizes (d_{50}) ~0.8 μm, 1.5 μm and 4 μm and Ag powder of particle size ~5 μm were used. The particle size distribution of the different WC starting powders, was measured by dynamic light scattering (Mastersizer Microplus, Malvern) and is plotted in Fig. 2. For this measurement, the WC powders were suspended in ethanol and a He–Ne laser light source ($\lambda = 632.8$ nm) was used to scatter the light from the particles. For the 0.8 μm WC, the distribution is negatively skewed whereas the distribution is more positively skewed for the 1.5 μm and 4 μm WC powders. To investigate the morphology of the particles, the powder was suspended in ethanol and de-agglomerated using ultrasonic vibration. A drop of the suspension was dried on an aluminum substrate, which was observed under a scanning electron microscope (XL30-FEG, FEI). Secondary electron micrographs of the different WC powders are shown in Fig. 3. The WC particles are non-spherical and tend to form agglomerates because of their inherent non-spherical morphology and propensity to minimize their surface energy by adhering to other particles.

The amount of porosity in the sintered pellet was carefully engineered in order to result in a desired final composition with 50, 55 or 60 wt.% Ag after infiltration. When targeting a final Ag content

Table 1
Summary of relevant switching tests performed for Ag–WC contact materials in AC (Nomenclature of switching conditions is given in Table 2).

Contact material/Composition (wt.%)	Type of switching test	Switching conditions	Focus	Key conclusions	Ref.
Ag–WC: 60–40 Ag–WC: 50–50 Ag–WC: 35–65	Break-only in air	$U = 230$ V, 50 Hz $\hat{i} = 1300$ A $n = 50$ $\cos\phi = 0.35$	Arc erosion, contact resistance	Arc erosion: Ag–WC: 60–40 < 50–50 < 35–65 Contact resistance: Ag–WC: 60–40 = 50–50 < 35–65 Surface layers: W, tungsten oxide and silver tungstate increase R_C	[1]
Ag–WC 60–40 Structure Dopant A Medium 1.8 B Coarse 1.8 C Fine 0.1	Break-only in air	$U = 230$ V, 50 Hz $\hat{i} = 1300$ A $n = 50$ $\cos\phi = 0.35$	Arc erosion, contact resistance	Arc-erosion: A = B = C Contact resistance: A = B > C Less dopant amount leads to lower contact resistance independent of microstructure.	[2]
Ag–WC–Co: 30–68–2 Ag–WC: 40–60 Ag–WC–Zr: 39.5–60–0.5	Break-only in vacuum (5×10^{-7} mbar)	$U = 400$ V AC $\hat{i} = 1500$ A $n = 1000$ $\cos\phi = 0.35$	Current chopping, contact erosion	On the contact surface Ag–WC materials show distinct crack formation, droplets of splashed material and dust containing WC and Ag. Crack formation and dust particles reduced by addition of Zr	[4]
Ag–W: 50–50 Ag–W: 35–65 Ag–WC: 60–40	Break-only in air	$U = 220$ V, 50 Hz $\hat{i} = 60$ A–1800 A $n = 300$–1000 $I_m = 1$ A, 10 A, 20 A	Arc erosion, contact resistance	$\hat{i} = 350$ A: Semiconducting surface layers, $R_c\downarrow$ with $I_m\uparrow$ $\hat{i} = 1000$ A: No layers (metallic contact), $R_c\uparrow$ with $I_m\uparrow$ Reduced arc erosion corresponds to increased R_C.	[20]
Ag–W: 35–65 Ag–WC: 40–60 Ag–Mo: 50.7–49.3	Toggle switch in air	$U = 110$ V, 60 Hz $i_{rms} = 30$ A $n = 2000$ $I_m = 30$ A $\cos\phi = 1$	Arc erosion, contact resistance	Arc erosion: Ag–W > Ag–WC > Ag–Mo Contact resistance: Ag–W > Ag–Mo > Ag–WC	[21]

of 60 wt.%, it was reasonable to start with an initial starting powder mixture with a Ag content of 40 wt.%. A very small amount of Ni (0.1 wt.%) was added to the powder mixture of Ag and WC to improve the sintering activity [22,23], allowing to sinter the powder just above the liquidus of silver. A stable porous skeleton of Ag and WC was formed by uniaxial compaction followed by sintering in reducing atmosphere (H_2). Then it was infiltrated with silver well above the liquidus in H_2 atmosphere to achieve near theoretical density. The final composition of the infiltrated discs was varied by changing the pressure during uniaxial compaction and the starting powder composition, which would lead to distinct sintering shrinkage. After full densification of the pellets by Ag infiltration, they were brazed on a copper support and turned down to Ø = 4 mm for further testing.

2.2. Metallographic preparation

Due to the large difference in hardness between silver and tungsten carbide, a conventional metallographic preparation is not suitable. Smearing of ductile silver, selective grinding away of silver, plucking out of tungsten carbide particles and a wavy surface finish are common problems associated with surface preparation. A single step grinding process which is known for providing high material removal rate, perfect flatness and optimum edge protection was applied using an MD-Allegro™ (Struers) grinding disc. The grinding process was carried out for 10 min at 150 rpm with a 15 μm diamond suspension (Kemet). It replaced several grinding steps on SiC paper which would result in more selective erosion of silver and other metallographic artifacts. After ensuring a flat surface post grinding, the composites were polished using different diamond suspensions from the coarsest to the finest (6 μm to 1 μm) for 5 min each at 150 rpm. OP-S, colloidal silica suspension (Struers) was used for the final polishing step for 2 min at 150 rpm.

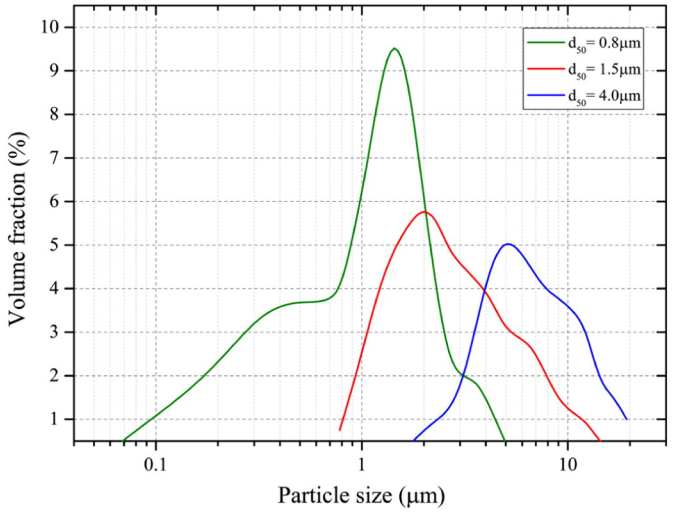

Fig. 2. Particle size distribution of the three different WC starting powders.

2.3. Break-only model switch

In the present work, a break-only test has been used to characterize the switching behavior of the contacts. The test is inspired by Sequence X of U.L. 489 [24], where the contacts should operate at an overrated current of 6 times rated current for 50 operations. After the overload switching sequence, the terminals of the device should not exceed a 50 °C rise above ambient while carrying rated current. However, instead of measuring the temperature rise, the electrical contact resistance was measured, as temperature rise is a function of device design (venting and heat conduction).

In this test, two identical contacts were brought together and a half sinusoidal current wave front having a frequency of 50 Hz was passed through it (Fig. 4.a). Then they were opened at the beginning of the sinusoidal current (natural current zero) and the current flowed for one half-cycle to observe an arc in-between the contacts, until next current zero (Fig. 4.b). Due to some mechanical delay (<1 ms), the duration of the arc was less than 10 ms. After the arc extinguished at current zero the electrical circuit was interrupted by a thyristor. Then the contacts were re-closed for electrical contact resistance measurement, during which the voltage drop across the contacts was measured using a direct current of 10 A (Fig. 4.c). Thereafter, the sinusoidal voltage was applied and the controller started to open the contacts again and this controlled sequence was carried out for 50 switching operations. The direction of the current flow was alternated after every switching cycle to avoid material transfer influences. The applied experimental parameters in the test are summarized in Table 2 [1,2].

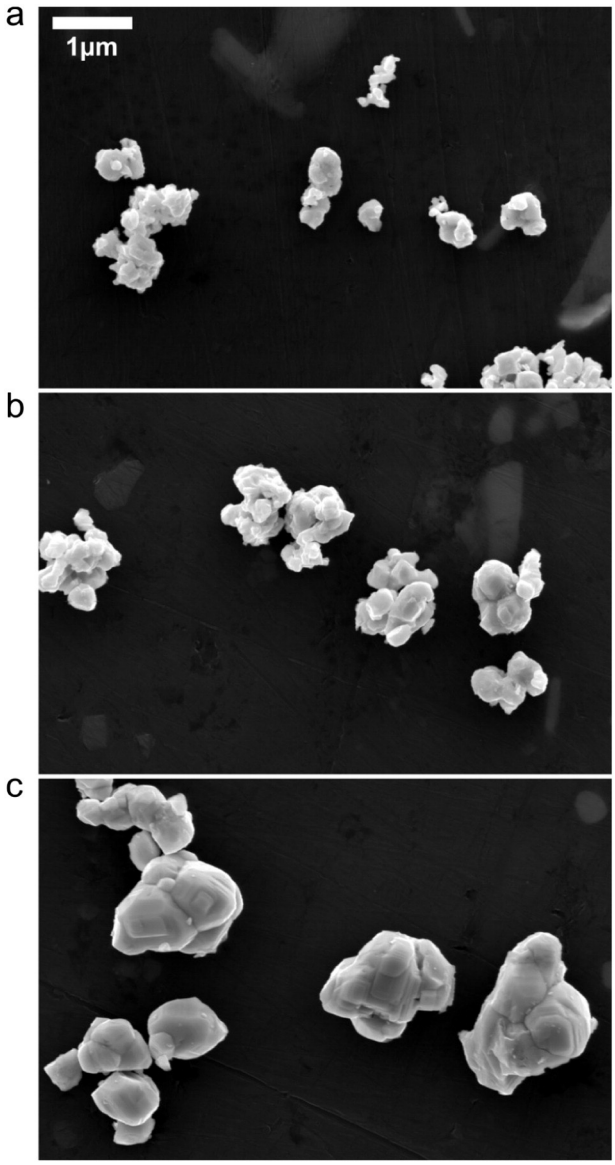

Fig. 3. Secondary electron images of the WC powders with a specified particle size of (a) 0.8 μm, (b) 1.5 μm and (c) 4 μm.

2.4. Thermal conductivity calculations using OOF2

In this study, two-dimensional backscattered electron images, as shown in Fig. 6, were first converted into binary images. This allowed easy classification of two "pixel groups" in terms of contrast and individual phases, as in this case silver and tungsten carbide. Thermal conductivity, *k*, values as a function of temperature were assigned to both silver [25] and tungsten carbide [26] pixel groups. In this model, a thermal gradient is simulated in the vertical direction of the image by assigning the top boundary 10 K higher than the bottom boundary and keeping both left and right boundaries adiabatic. The thermal gradient orientation in the microstructure was kept consistent with that in the switching test. Such a small gradient was deliberately chosen to allow using the *k* values of individual phases for that particular temperature range, i.e. when the top boundary was kept at 505 °C and the bottom boundary was kept at 495 °C, the *k* values at 500 °C were used. Triangular elements were used to build up the FE mesh, which adapted the microstructure where the mesh boundary would snap to the "pixel group" and emphasize more on the shape of the particles than the homogeneity of the mesh.

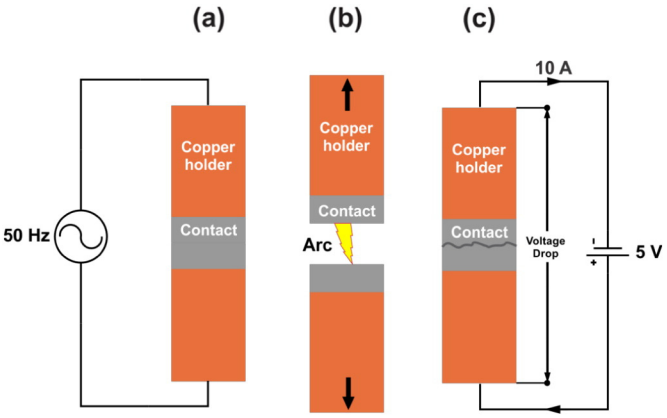

Fig. 4. Break-only switching test sequence.

After setting the boundary conditions and creating a FE mesh, the heat flux equation was solved by the conjugate gradient method resulting in flux components at each node assuming steady-state heat conduction. The heat flux at the top and bottom were calculated by integrating the flux values at all the nodes at the top and bottom respectively. The effective thermal conductivity, *k*, was calculated using the Fourier's law of heat conduction

$$k = \frac{Q/x}{(T_{top} - T_{bottom})/y} \tag{2.1}$$

where *Q* is the average of the integrated flux at the top and bottom boundary, x and y are image dimensions and $(T_{top} - T_{bottom})$ is the applied thermal gradient. The effective thermal conductivity values were calculated for temperatures from 300 to 1200 K.

3. Results and discussion

3.1. Initial microstructure and hardness

Representative microstructures after sintering followed by infiltration are presented for a material containing 60 wt.% of Ag and WC particle size of 0.8 μm. Fig. 5 illustrates the backscattered electron (BSE) images which exhibit atomic number contrast between Ag and WC, where the bright phase corresponds to WC and the dark phase corresponds to Ag. The residual porosity indicated in Fig. 5(a) is filled with silver during infiltration as shown in Fig. 5(b).

As previously illustrated in Fig. 4, the break-only test requires an identical contact pair. Four composites were therefore produced for each silver content and WC particle size to perform two switching tests. The final silver content is a function of the sintered density of the composites, which is dependent on the applied uniaxial pressure. The calculated silver contents are tabulated in Table 3 which also shows that it is difficult to obtain identical compositions and thus a standard error has been assigned to each composite. Transverse cross-sections of the discs (plane, parallel to the direction of infiltration) were prepared and characterized. Fig. 6 illustrates the different Ag–

Table 2
Test parameters of the break-only model switch.

Test parameters	Value
Voltage *U*	230 V
Peak current $\hat{\imath}$	1300 A
Power factor $cos\phi$	0.35 ± 0.05
Contact opening velocity *v*	0.4 ms^{-1}
Number of operations *n*	50
Contact load *F*	20 N
R_c measuring current I_m	10 A

WC grades prepared by infiltration having different final silver contents and WC particle sizes.

One of the salient features is that the silver matrix appears to be more continuous for the coarsest WC grades than for the finer WC grades. This percolating silver is a result of the non-agglomeration of the coarse WC particles which do not form necks at such low temperatures due to the lower driving force for sintering.

The hardness of the infiltrated composites was measured using a Vickers hardness tester (Model FV-700, Future-Tech Corp., Tokyo, Japan) with a load of 0.3 kgf and a dwell time of 10 s. Fig. 7 shows the evolution of the hardness as a function of the silver content and WC particle size. The standard error of mean associated to the silver content is tabulated in Table 3 and the standard error of mean in the hardness is based on six measurements. It is clear that the hardness decreases with increasing silver content and increasing WC particle size. To give some knowledge about the flow stress of the contacts, the yield strength was calculated using an empirical relationship which holds true for several materials [27–29]. However, as mentioned before, the primary knowledge of the hardness is useful but the evolution of the surface morphology during operation is more interesting from a design perspective.

Table 3
WC particle size and average silver content of the infiltrated composites before switching. The corresponding microstructures are shown in Fig. 6.

Sample number	WC particle size (μm)	Silver content (wt.%)				
		Test 1		Test 2		Average Ag content
		Upper contact	Lower contact	Upper contact	Lower contact	
a1	0.8	51.24	50.66	50.48	50.41	50.70 ± 0.19
a2	0.8	55.84	55.67	55.76	56.20	55.87 ± 0.12
a3	0.8	60.88	60.46	60.68	60.70	60.68 ± 0.09
a4	0.8	65.18	64.81	65.49	65.32	65.20 ± 0.14
a5	0.8	68.74	69.10	68.89	68.92	68.91 ± 0.07
b1	1.5	49.89	50.36	49.67	50.41	50.08 ± 0.18
b2	1.5	55.34	55.09	55.40	55.31	55.29 ± 0.07
b3	1.5	60.66	60.53	60.50	60.70	60.60 ± 0.05
b4	1.5	64.63	64.60	64.47	64.34	64.51 ± 0.07
c1	4	50.78	50.27	49.98	49.59	50.16 ± 0.25
c2	4	55.00	55.07	54.66	55.11	54.96 ± 0.10
c3	4	59.87	60.15	59.98	60.20	60.05 ± 0.08

3.2. Contact resistance measurement

Contacts with various silver content and different WC particle size were densified using press–sinter–infiltration (Fig. 6) and the electrical contact resistance (R_c) between two similar contacts were measured during 50 switching operations, as explained in Section 2.3. Four samples were produced for each silver content and WC particle size to test the switching properties of two contact pairs. Fig. 8(a) shows the effect of composition on the contact resistance for a 0.8 μm WC composite. Since two tests were performed under identical conditions, the plotted data in Fig. 8(a) are the average of two tests and the error bar represents the scatter between two tests. It is clear that the contact resistance decreases with increasing silver content from 50 to 70 wt.%. Before arcing, the resistance is very low and in the order of 0.2 m Ω and the difference for different silver contents is not appreciable. After a certain number of switching cycles, the resistance becomes stable and the scatter is within an acceptable limit. Fig. 8 (b–d) shows the influence of the WC particle size on the contact resistance for three different compositions. Here the scatter between the two tests is not displayed, since from Fig. 8(a) we know that the differences are very small. The most striking feature is the very low and stable contact resistance for the composite with the coarsest WC grade.

The number of cycles required to establish a stable contact resistance value differs from material to material. The ramp of increasing R_c ends after approximately 5 switching cycles for the finer grade of tungsten carbide whereas this is about 10 cycles for the coarser WC grade (Fig. 8(b)).

For comparing several composites, it is easier to compare the mean of the resistance values, but such an approach should be adopted only after the resistance reaches a stable value. Since R_c was observed to become stable after 10 cycles for most materials, the data were averaged over cycles 11–50 and plotted against the silver content and WC particle size in Fig. 9. The standard error of mean (R_c) value is appreciably small which makes it a reasonable assumption to eliminate the first 10 data points. The overview in Fig. 9 indicates a sharp drop in contact resistance in between 50 and 55 wt.% (60 and 64.6 vol.%) of silver for a WC particle size of 4 μm and between 55 and 60 wt.% (64.6 and 69 vol.%) of silver for a WC particle size of 0.8 and 1.5 μm. This confirms the onset composition of percolation, where the Ag matrix becomes completely interconnecting. For a fixed composition, a drop in contact resistance is essentially observed between WC particle sizes of 1.5 and 4 μm which also mark a percolation threshold. However, the surface layers formed after arcing strongly influence the contact resistance since we always observe an increase in R_c in the first 5–10 cycles due to the degradation of the contact surface. After the arc strikes, the silver in the matrix vaporizes and then re-solidifies after the arc-extinguishes, on top of the sintered WC particles which would form on the surface. Coarser tungsten carbide forms a more ductile sintered network than the finer tungsten carbide and thus allows more area of true mechanical contact (A_c) which leads to a lower contact resistance (Eq. (1.4)).

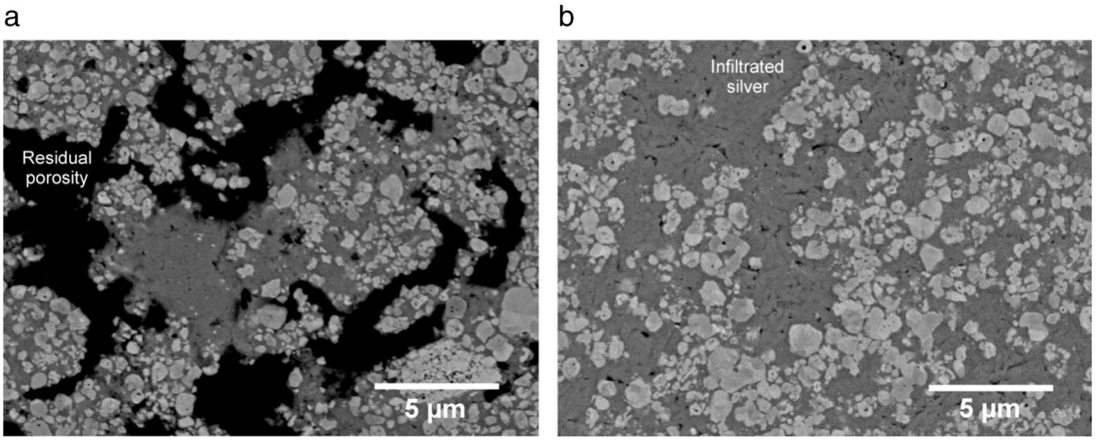

Fig. 5. Backscattered electron micrographs after (a) pressing and sintering; (b) after infiltration for a material containing 60 wt.% of Ag and WC particle size of 0.8 μm.

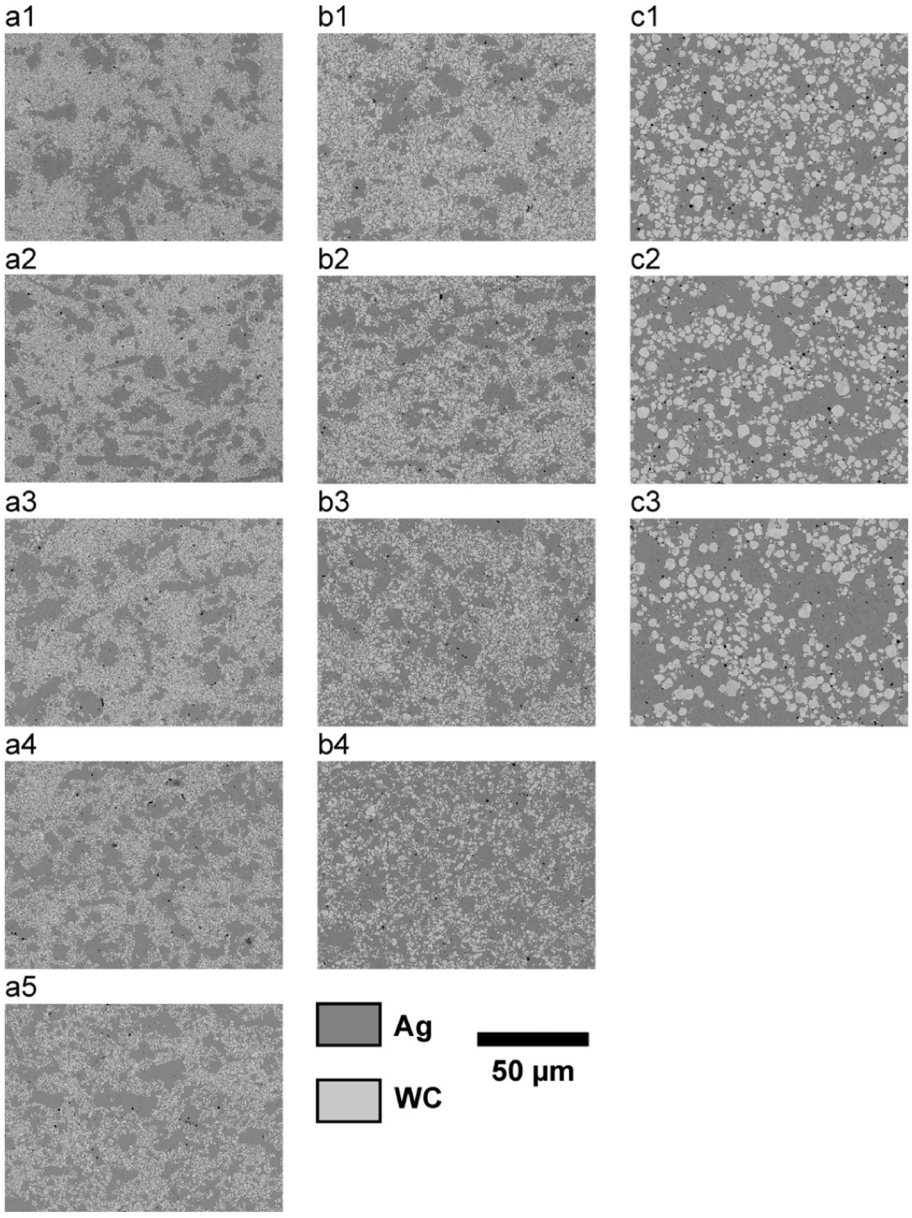

Fig. 6. Backscattered electron micrographs of the infiltrated Ag–WC materials with different Ag content and WC particle size. The figure numbers refer to the sample numbers in Table 3.

3.3. Microstructure after switching

After 50 switching operations, the contact pair was appreciably eroded. To capture the complete profile of the contact surface after switching, confocal laser scanning microscopy was used to scan through the whole surface as shown in Fig. 10. The surface essentially consists of re-condensed silver and molten tungsten carbides which form small lakes and discrete globules respectively. It also contains different oxides of tungsten which form a thin coating as a result of condensation of the volatile oxides. Tungsten forms four oxides WO_3 (yellow), $WO_{2.9}$ (blue), $WO_{2.72}$ (violet) and WO_2 (brown) which can be distinguished by their color [30]. Fig. 10 clearly shows the formation of two different oxides, which have blue (non-stoichiometric) and yellow (stoichiometric) color. To have a better understanding of the effect of arcing on the microstructure, the transverse section of the contact (parallel to the direction of arcing) was prepared for metallographic examination as elaborated in Section 2.2.

Fig. 11 shows a series of micrographs of the transverse section illustrating the aftermath of arcing. The backscattered electron micrographs show different phase contrast as explained below. The contacts were mounted on an epoxy resin (■) for metallographic preparation. The darker phase indicates silver (■) in all the figures except for Fig. 11 (a1), where the copper carrier has the darkest contrast and the brighter phase corresponds to WC (■). The brightest phase corresponds to W_2C, as explained below.

The contacts exhibit several defects like cracks, gas bubbles, porosity and re-condensed material as shown in Fig. 12. Thermal stress cracking behavior in silver-refractory contact materials has been studied before by Wingert [31]. Cracks formed during the electric arcing generally had two orientations, i.e., perpendicular or parallel to the face of contact, which was also observed in this study. When these two crack orientations intersect, it would lead to the loss of a large part of the contact leading to high arc-erosion. Apart from erosion, cracks can lead to a thermal and electrical barrier within the contact piece leading to higher

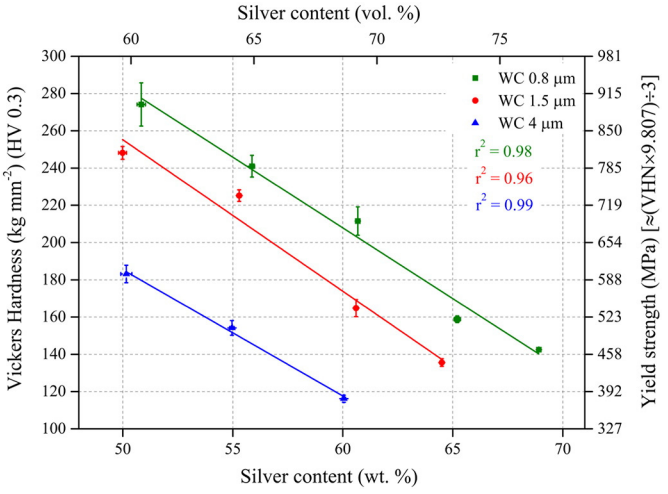

Fig. 7. Hardness and calculated yield strength as a function of silver content and WC particle size.

contact resistance which is reflected in the temperature rise as a consequence of joule heating.

In this context, thermal tensile stresses are potential causes for crack initiation and propagation. Thermal shock induced cracking is an inevitable consequence observed in ceramics and ceramic containing

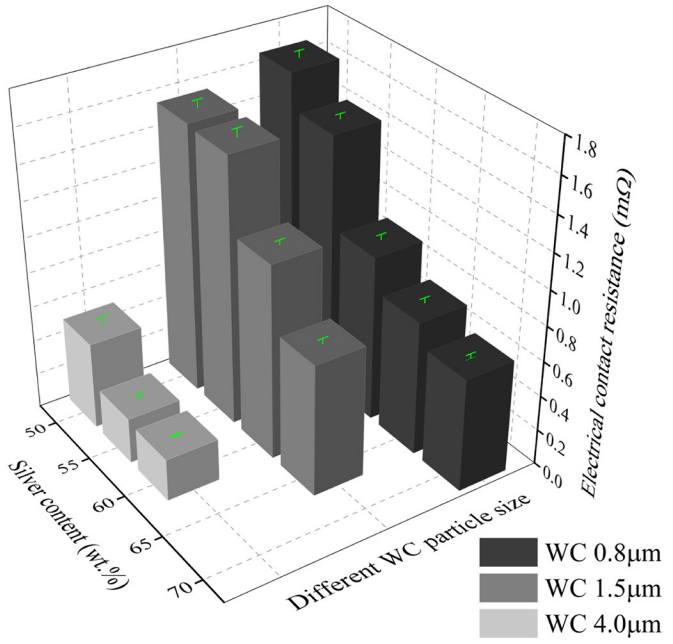

Fig. 9. Averaged electrical contact resistance from cycle 11 to 50 for different Ag contents and WC particle sizes.

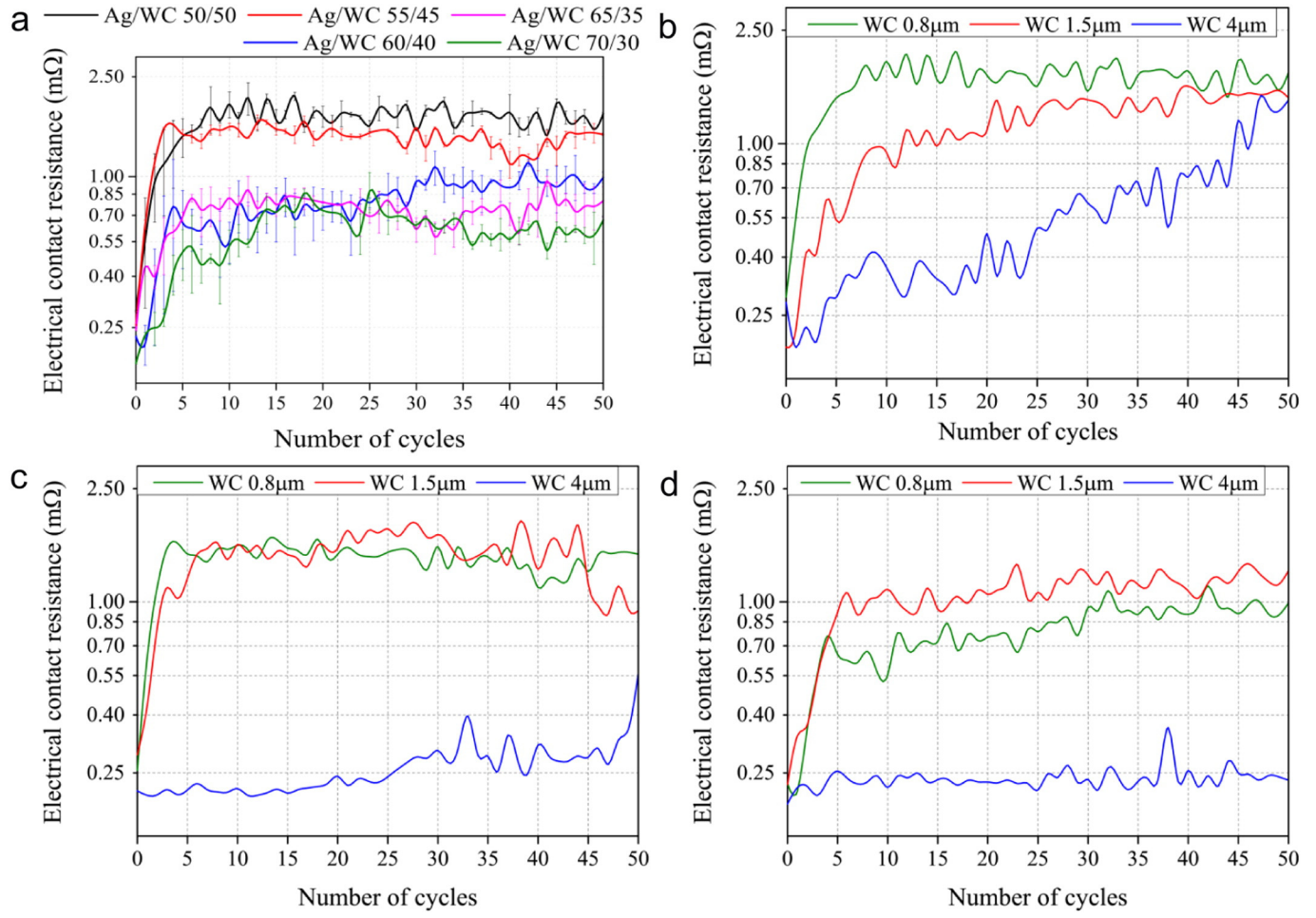

Fig. 8. Evolution of R_c over 50 cycles (a) for different silver containing materials for WC 0.8 μm and for different WC particle sizes having (b) Ag–WC 50–50 (wt.%), (c) Ag–WC 55–45 (wt.%) and (d) Ag–WC 60–40 (wt.%).

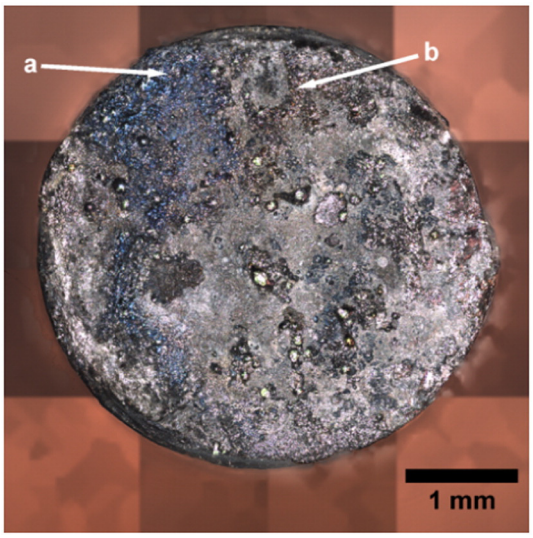

Fig. 10. Representative contact surface after 50 switching operations. (a) Thin film of non-stoichiometric tungsten oxide (blue) and (b) thin film of stoichiometric tungsten oxide (yellow). (For interpretation of the references to color in this figure legend, the reader is referred to the web version of this article.)

composites operating at high temperatures. The thermal gradient, as a result of low thermal conductivity, causes expansion in different proportions within the sample. In ceramic composites, a thermal gradient also arises due to the contrasting thermal expansion coefficients of the constituent phases. The thermal shock parameter (R) of a material, i.e. the maximum temperature gradient $(\Delta T)_{max}$, a material can withstand without crack formation is estimated as

$$R = (\Delta T)_{max} = \frac{k\sigma_f C}{E\alpha}. \tag{3.1}$$

The thermal gradient causing the shock is essentially influenced by the thermal conductivity of the composite (k), failure strength (σ_f) (which for ceramics is often taken as the flexural strength or MOR), Young's modulus (E), coefficient of thermal expansion (α) and constraint (C) where $C = 1$ for axial constraint, $(1 - \nu)$ for biaxial constraint or normal quenching, and $(1 - 2\nu)$ for triaxial constraint, where ν is the Poisson's ratio [32].

The thermal conductivity of the different Ag–WC composites was calculated based on their actual microstructure as a function of temperature as explained in Section 2.4.

It is quite evident from Fig. 13 that the effective thermal conductivity decreases with increasing temperature and decreasing WC particle size. This is a direct consequence of the area fraction of phase/grain boundaries and the homogeneity of the dispersed phase. More grain and phase boundaries result in a higher resistance to heat flow due to the lower mobility of the heat carriers across the boundaries and through the WC grains. Again, a very homogeneous dispersion of the WC phase would also result in a higher conductivity as the carriers can transfer through the higher conductive phase. The standard error associated with each measurement (see Fig. 13) is the difference between the integrated flux on the top and bottom, which otherwise should be zero assuming steady-state calculation.

Fig. 14 (a–c) shows the meshing in the OOF2 software, which adapts according to the microstructure. The mesh is refined near the boundaries and phases of small dimensions. Fig. 14 (d–f) shows the heat flux map which gives an idea about the heat flow under the simulated thermal gradient. It is quite evident from the map that the heat carriers find an easy route through the percolating silver phase in the material having the coarsest WC (4 μm).

The thermal conductivity results can be used to explain the cracks formed during switching. After switching, the coarsest WC grain materials did not show any crack formation for both low and high silver contents (Fig. 11 (c1–c3)). However, fine WC grain composites showed cracks even for the highest silver content (Fig. 11 (a1–a5)). This correlates with the effective thermal conductivity calculations of the composites, where the less thermally conducting composite has the lowest thermal shock resistance. Larger WC particles sometimes also act as a reinforcing phase and inhibit the crack to propagate. Apart from the material properties, the microstructural length scale in the composite materials containing ductile and brittle phases determines the resistance against crack propagation [33].

Figs. 11 (c3) and 15 show another characteristic microstructural feature where the open cracks are infiltrated with silver during switching. This phenomenon was also observed by Wingert [31] for Ag–W contact materials. Two possible reasons were proposed to explain the above effect, i.e. the capillary effect and/or the volume expansion of Ag upon melting drives the molten silver into the narrow cracks. The first explanation is more plausible in this case since the wider cracks were not filled with silver due to the lower capillary forces. This process of self-healing is very useful as it improves the silver interconnecting network and glues together the broken pieces of the composite.

Another microstructural feature, not reported previously, was the formation of tungsten rich carbides on top of the contact surface. Fig. 12 shows the formation of W_2C in the shape of a globule. The chemical composition of the above phase was measured to be 93.64 ± 0.34 wt.% or 65.24 ± 1.81 at.% W and 3.27 ± 0.27 wt.% or 34.76 ±

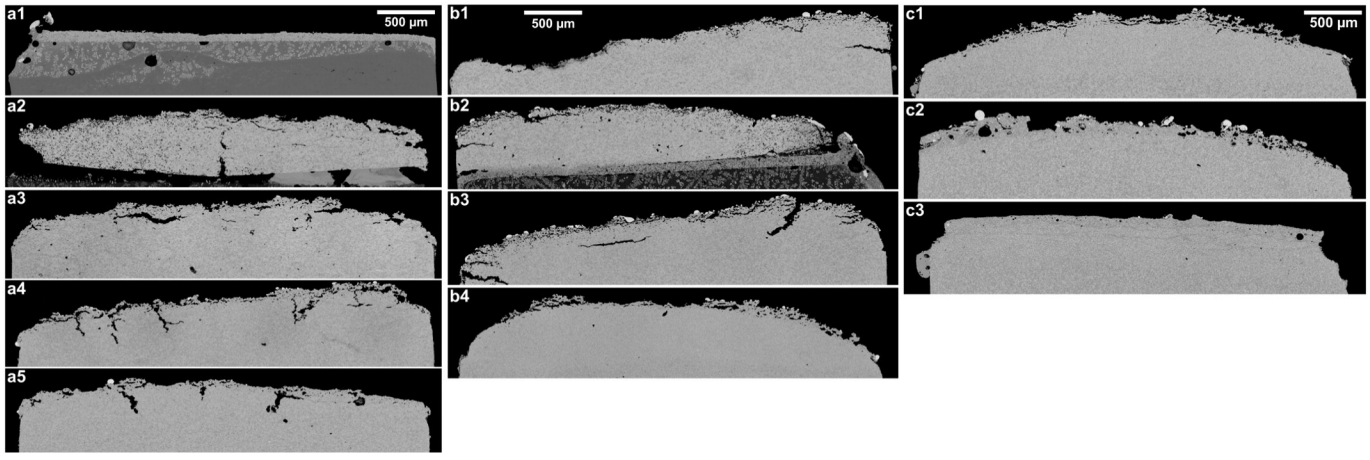

Fig. 11. Transverse section of the contacts after 50 switching operations for the composites with WC particle size of (a1–a5) 0.8 μm; (b1–b4) 1.5 μm; and (c1–c3) 4 μm; for composition of (a1–a5, b1–b4, c1–c3) refer to Table 3; sample a1 was eroded completely.

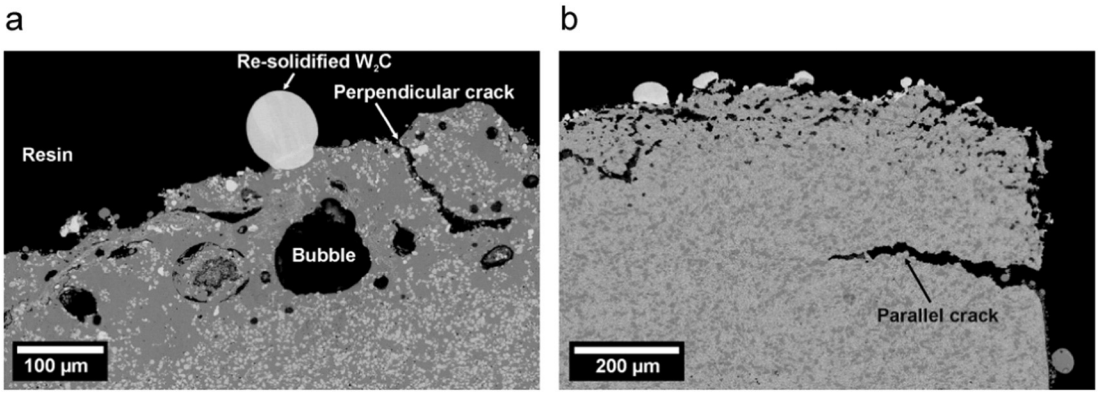

Fig. 12. Characteristic surface damages after 50 switching operations (a) magnified image of Fig. 11 (c2) and (b) magnified image of Fig. 11 (b1).

1.81 at.% C by means of wavelength dispersive spectroscopy (WDS). The shape of the bright phase suggests that the WC was first molten and re-solidified as W_2C. This indicates that the temperature of the contact surface even rises above the melting point of W_2C (2785 °C). W_2C is a metastable carbide and covers a wide composition range in the tungsten–carbon phase diagram [34]. Thus its formation is quite probable for such a fast kinetically driven process. It is more brittle than WC and could be detrimental for the contacts when formed in large quantities.

4. Conclusions

Ag–WC composites were successfully prepared by liquid phase sintering followed by infiltration of silver. The composition of the pellets was varied by adjusting the compaction pressure prior to sintering, which allowed different porosity volume fractions to be subsequently infiltrated with silver. The evolution of the electrical contact resistance, R_c, during switching and the microstructures before and after switching

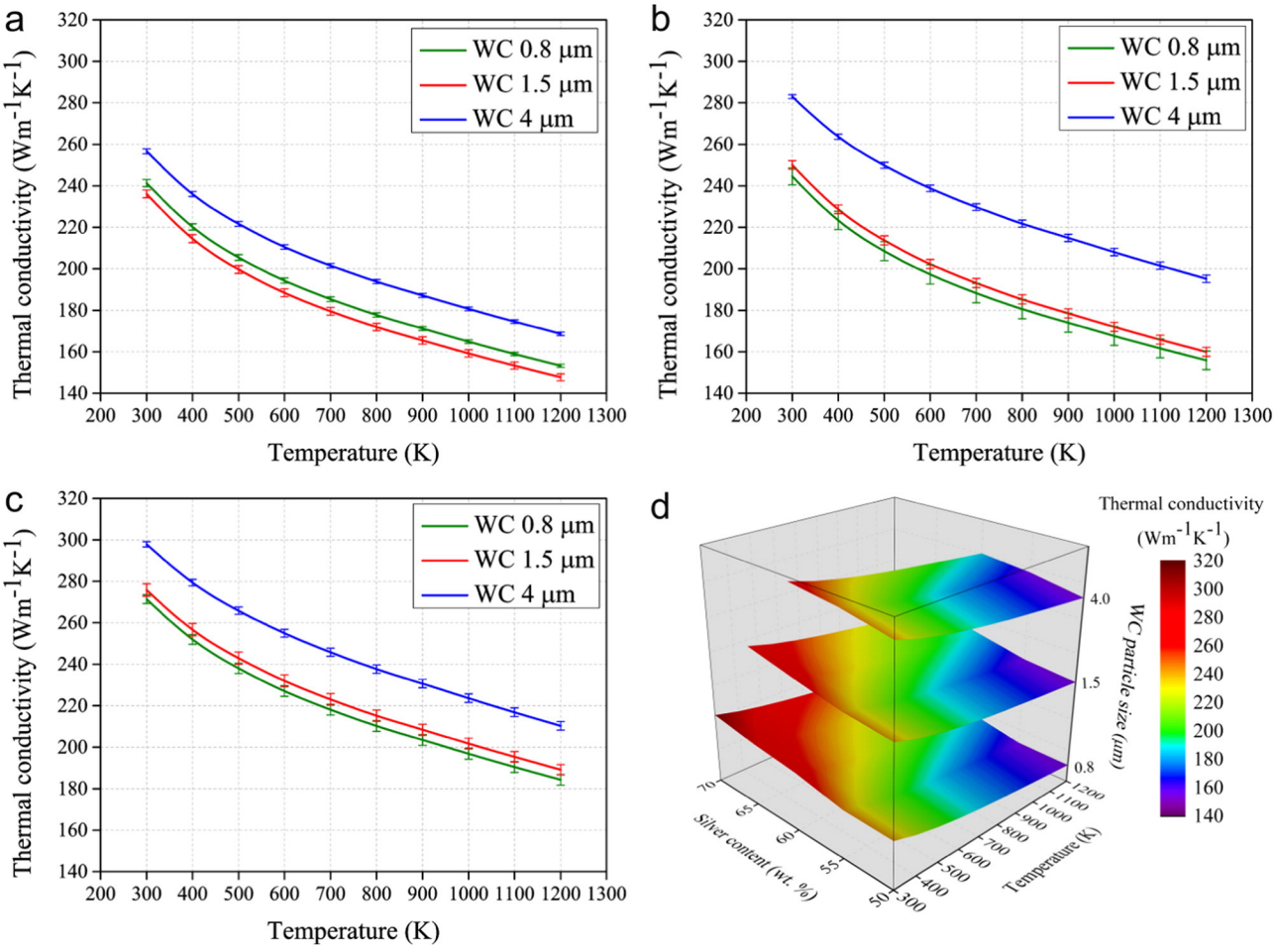

Fig. 13. OOF2 calculated thermal conductivity values as a function of temperature for (a) Ag–WC 50–50 (wt.%), (b) Ag–WC 55–45 (wt.%), (c) Ag–WC 60–40 (wt.%) and (d) for five compositions and three WC particle sizes.

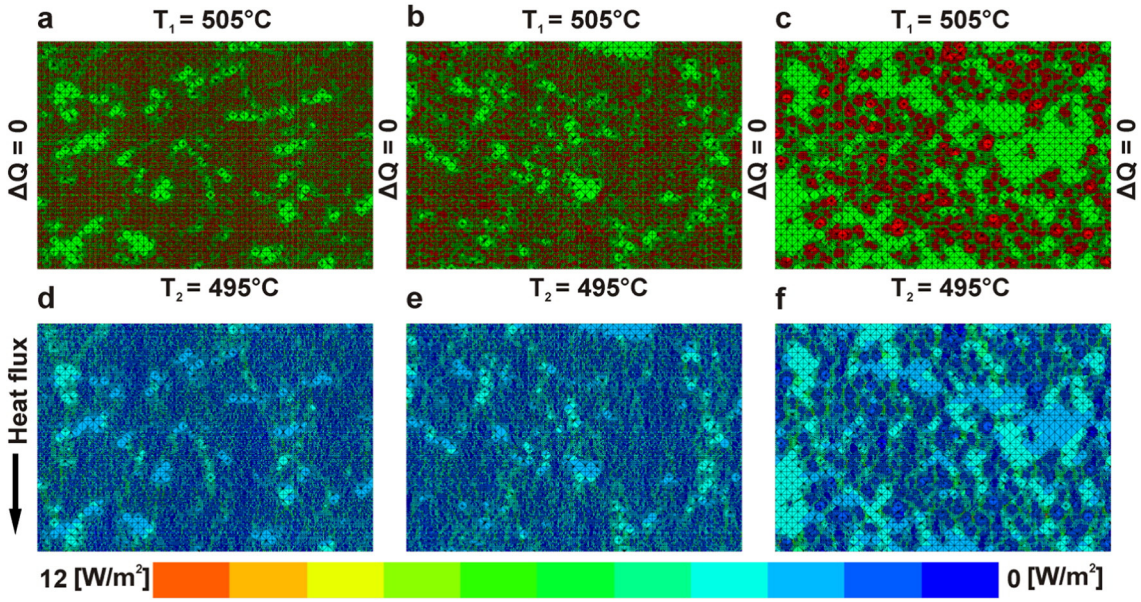

Fig. 14. OOF2 meshing of Ag (green)–WC (red) 60–40 (wt.%) materials for (a) WC 0.8 μm, (b) WC 1.5 μm and (c) WC 4 μm. Corresponding heat flux map for Ag–WC 60–40 (wt.%) (d) WC 0.8 μm, (e) WC 1.5 μm and (f) WC 4 μm as a result of the thermal gradient imposed from top to bottom, keeping the sides adiabatic. All images are 125 μm × 94 μm. (For interpretation of the references to color in this figure legend, the reader is referred to the web version of this article.)

elucidates the material behavior and allows one to draw the following conclusions:

1. In contrast to 0.8 μm WC particles, 4 μm WC grains tend to agglomerate less during sintering, resulting in a more continuous silver network in the composite. This improves the initial thermal and electrical conductivity and ductility.
2. A direct correlation was established between the electrical contact resistance (R_c), the WC particle size and the composite composition. A drop in contact resistance (~1.2 m Ω) was observed by adding 4 μm instead of 0.8 μm WC at a silver content of 50 wt.% and a drop of ~1 m Ω was observed by increasing the silver content up to 70 wt.% in a 0.8 μm WC composite. This could be explained phenomenologically from a combined effect of the percolating silver matrix and the flow stress of the surface layer. Above the percolating limit, the R_c dropped by 0.5 m Ω for the 0.8 μm WC composite with >55 wt.% of Ag, whereas the R_c dropped by 0.25 m Ω for the 4 μm WC composite with >50 wt.% of Ag. For a more ductile surface layer, the true mechanical contact would be larger which decreases the R_c considerably.
3. Microstructural investigation accompanied with 2D microstructure based modeling of the fabricated Ag–WC composites divulged the relationship between the thermal stress induced fracture, WC particle size and Ag content. The thermal shock resistance of these materials is strongly influenced by its thermal conductivity, which was calculated as a function of temperature, WC particle size and Ag–WC composition. This study revealed that the thermal shock resistance increased due to an increased thermal conductivity for Ag–WC composites with coarser WC grains or a higher silver content.

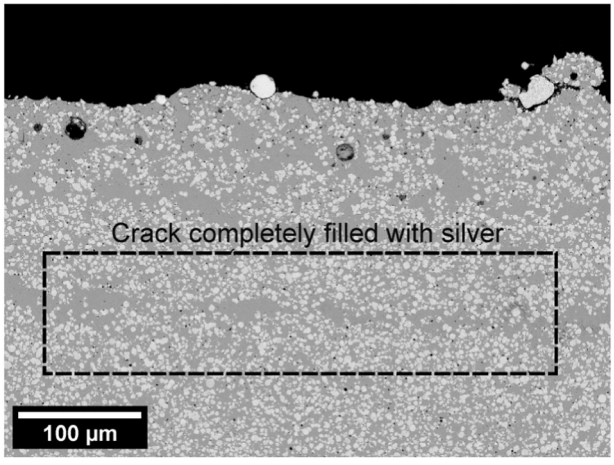

Fig. 15. Cracks filled with silver (magnified image of Fig. 11 (c3)).

Appendix A. Supplementary data

Supplementary data to this article can be found online at http://dx.doi.org/10.1016/j.matdes.2015.07.006.

References

[1] T. Mützel, R. Niederreuther, Development of contact material solutions for low-voltage circuit breaker applications (2), 2011 IEEE 57th Holm Conference on Electrical Contacts (Holm), Minneapolis, MN, USA 2011, pp. 1–6, http://dx.doi.org/10.1109/HOLM.2011.6034790.
[2] T. Mützel, B. Kempf, Silver tungsten carbide contacts for circuit breaker applications, 2014 IEEE 60th Holm Conference on Electrical Contacts (Holm) 2014, pp. 1–7, http://dx.doi.org/10.1109/HOLM.2014.7031059.
[3] C.-H. Leung, Contact materials, silver graphite, silver-refractory-graphite, in: Q.J. Wang, Y.-W. Chung (Eds.), Encyclopedia of Tribology, Springer US 2013, pp. 468–470.
[4] V. Behrens, T. Honig, A. Kraus, Tungsten and tungsten carbide based contact materials used in low voltage vacuum contactors, Proceedings of the Forty-Fifth IEEE Holm Conference on Electrical Contacts, 1999, Pittsburgh, PA, USA 1999, pp. 105–110, http://dx.doi.org/10.1109/HOLM.1999.795934.
[5] M. Vijayakumar, A.M. Sriramamurthy, S.V. Nagender Naidu, Calculated phase diagrams of Cu–W, Ag–W and Au–W binary systems, Calphad 12 (1988) 177–184, http://dx.doi.org/10.1016/0364-5916(88)90019-3.
[6] P.G. Slade, Electrical Contacts: Principles and Applications, CRC Press, 1999.
[7] J.A. Greenwood, Constriction resistance and the real area of contact, Br. J. Appl. Phys. 17 (1966) 1621, http://dx.doi.org/10.1088/0508-3443/17/12/310.
[8] R. Landauer, The electrical resistance of binary metallic mixtures, J. Appl. Phys. 23 (1952) 779–784, http://dx.doi.org/10.1063/1.1702301.
[9] G. Bánhegyi, Comparison of electrical mixture rules for composites, Colloid Polym. Sci. 264 (1986) 1030–1050, http://dx.doi.org/10.1007/BF01410321.
[10] S. Kirkpatrick, Percolation and conduction, Rev. Mod. Phys. 45 (1973) 574–588, http://dx.doi.org/10.1103/RevModPhys.45.574.
[11] D.S. McLachlan, M. Blaszkiewicz, R.E. Newnham, Electrical resistivity of composites, J. Am. Ceram. Soc. 73 (1990) 2187–2203, http://dx.doi.org/10.1111/j.1151-2916.1990.tb07576.x.

[12] F. Findik, H. Uzun, Design Materials, Microstructure, hardness and electrical properties of silver-based refractory contact materials, 24 (2003) 489–492, http://dx.doi.org/10.1016/S0261-3069(03)00125-0.
[13] A.C.E. Reid, S.A. Langer, R.C. Lua, V.R. Coffman, S.-I. Haan, R.E. García, Image-based finite element mesh construction for material microstructures, Comput. Mater. Sci. 43 (2008) 989–999, http://dx.doi.org/10.1016/j.commatsci.2008.02.016.
[14] A.C.E. Reid, R.C. Lua, R.E. Garcia, V.R. Coffman, S.A. Langer, Modelling microstructures with OOF2, Int. J. Mater. Prod. Technol. 35 (2009) 361, http://dx.doi.org/10.1504/IJMPT.2009.025687.
[15] J.P. Angle, Z. Wang, C. Dames, M.L. Mecartney, Comparison of two-phase thermal conductivity models with experiments on dilute ceramic composites, J. Am. Ceram. Soc. 96 (2013) 2935–2942, http://dx.doi.org/10.1111/jace.12488.
[16] K.E. Pappacena, M.T. Johnson, H. Wang, W.D. Porter, K.T. Faber, Thermal properties of wood-derived copper–silicon carbide composites fabricated via electrodeposition, Compos. Sci. Technol. 70 (2010) 478–484, http://dx.doi.org/10.1016/j.compscitech.2009.11.011.
[17] Z. Wang, A. Kulkarni, S. Deshpande, T. Nakamura, H. Herman, Effects of pores and interfaces on effective properties of plasma sprayed zirconia coatings, Acta Mater. 51 (2003) 5319–5334, http://dx.doi.org/10.1016/S1359-6454(03)00390-2.
[18] J. Jaćimović, L. Felberbaum, E. Giannini, J. Teyssier, Electro-mechanical properties of composite materials for high-current contact applications, J. Phys. D. Appl. Phys. 47 (2014) 125501, http://dx.doi.org/10.1088/0022-3727/47/12/125501.
[19] P.G. Slade, Effect of the electric arc and the ambient air on the contact resistance of silver, tungsten, and silver-tungsten contacts, J. Appl. Phys. 47 (1976) 3438–3443, http://dx.doi.org/10.1063/1.323181.
[20] M. Lindmayer, M. Roth, Contact resistance and arc erosion of W/Ag and WC/Ag, IEEE Trans. Compon. Hybrid Manuf. Technol. 2 (1979) 70–75, http://dx.doi.org/10.1109/TCHMT.1979.1135414.
[21] C.-H. Leung, H. Kim, A comparison of Ag/W, Ag/WC, and Ag/Mo electrical contacts, IEEE Trans. Compon. Hybrid Manuf. Technol. 7 (1984) 69–75, http://dx.doi.org/10.1109/TCHMT.1984.1136333.
[22] H.R. De Macedo, A.G.P. da Silva, D.M.A. de Melo, The spreading of cobalt, nickel and iron on tungsten carbide and the first stage of hard metal sintering, Mater. Lett. 57 (2003) 3924–3932, http://dx.doi.org/10.1016/S0167-577X(03)00242-8.
[23] N.M. Hwang, Y.J. Park, D.-Y. Kim, D.Y. Yoon, Activated sintering of nickel-doped tungsten: approach by grain boundary structural transition, Scr. Mater. 42 (2000) 421–425, http://dx.doi.org/10.1016/S1359-6462(99)00344-9.
[24] U.L. 489 Molded-Case Circuit Breakers, Molded-Case Switches, and Circuit Breaker Enclosures, 9th ed., 1996.
[25] R.W. Powell, C.Y. Ho, P.E. Liley, Thermal conductivity of selected materials, U.S. Dept. of Commerce, National Bureau of Standards; for sale by the Superintendent of Documents, U.S. Govt. Print. Off, 1966.
[26] A. Gubernat, P. Rutkowski, G. Grabowski, D. Zientara, Hot pressing of tungsten carbide with and without sintering additives, Int. J. Refract. Met. Hard Mater. 43 (2014) 193–199, http://dx.doi.org/10.1016/j.ijrmhm.2013.12.002.
[27] J.R. Cahoon, W.H. Broughton, A.R. Kutzak, The determination of yield strength from hardness measurements, MT 2 (1971) 1979–1983, http://dx.doi.org/10.1007/BF02913433.
[28] J.T. Busby, M.C. Hash, G.S. Was, The relationship between hardness and yield stress in irradiated austenitic and ferritic steels, J. Nucl. Mater. 336 (2005) 267–278, http://dx.doi.org/10.1016/j.jnucmat.2004.09.024.
[29] E.J. Pavlina, C.J.V. Tyne, Correlation of yield strength and tensile strength with hardness for steels, J. Mater. Eng. Perform. 17 (2008) 888–893, http://dx.doi.org/10.1007/s11665-008-9225-5.
[30] E. Lassner, W.-D. Schubert, Properties, Chemistry, Technology of the Elements, Alloys, and Chemical Compounds, Springer Science & Business Media, 1999.
[31] P.C. Wingert, Testing of the thermal-stress-cracking characteristics of silver-refractory contacts, Proceedings of the Forty-First IEEE Holm Conference on Electrical Contacts 1995, pp. 338–345, http://dx.doi.org/10.1109/HOLM.1995.482889.
[32] H.W. Stoll, Introduction to manufacturing and design, ASM Handbook Volume 20: Materials Selection and Design, 7, ASM International, 1997. 669–675.
[33] S. Schön, H. Prielipp, R. Janssen, J. Rödel, N. Claussen, Effect of microstructural scale on thermal shock resistance of aluminum-reinforced alumina, J. Am. Ceram. Soc. 77 (1994) 701–704, http://dx.doi.org/10.1111/j.1151-2916.1994.tb05352.x.
[34] A.S. Kurlov, A.I. Gusev, Tungsten carbides and W–C phase diagram, Inorg. Mater. 42 (2006) 121–127, http://dx.doi.org/10.1134/S0020168506020051.